Multi-physics corrosion modeling for sustainability assessment of steel reinforced high performance fiber reinforced cementitious composites

Lepech, M.; Michel, Alexander; Geiker, Mette

Published in:
Proceedings of the 9th International Conference on Fracture Mechanics of Concrete and Concrete Structures

Publication date:
2016

Document Version
Peer reviewed version

9th International Conference on Fracture Mechanics of Concrete and Concrete Structures
FraMCoS-9
V. Saouma, J. Bolander and E. Landis (Eds)

MULTI-PHYSICS CORROSION MODELING FOR SUSTAINABILITY ASSESSMENT OF STEEL REINFORCED HIGH PERFORMANCE FIBER REINFORCED CEMENTITIOUS COMPOSITES

M. LEPECH[*], M. GEIKER[†], AND A. MICHEL[††]

[*] Stanford University
Stanford, California, USA
e-mail: mlepech@stanford.edu

[†] Norwegian University of Science and Technology
Trondheim, Norway
e-mail: mette.geiker@ntnu.no

[††] Technical University of Denmark
Kgs. Lyngby, Denmark
e-mail: almic@byg.dtu.dk

Key words: Multi-physics, Corrosion, HPFRCC, Reinforced, Sustainability

Abstract: Using a newly developed multi-physics transport, corrosion, and cracking model, which models these phenomena as a coupled physiochemical processes, the role of HPFRCC crack control and formation in regulating steel reinforcement corrosion is investigated. This model describes transport of water and chemical species, the electric potential distribution in the HPFRCC, the electrochemical propagation of steel corrosion, and the role of microcracks in the HPFRCC material. Numerical results show that the reduction in anode and cathode size on the reinforcing steel surface, due to multiple crack formation and widespread depassivation, are the mechanism behind experimental results of HPFRCC steel corrosion studies found in the literature. Such results provide an indication of the fundamental mechanisms by which steel reinforced HPFRCC materials may be more durable than traditional reinforced concrete and other tension-softening cementitious composites. Finally, these results are extended to provide greater insight into the assessment and design of more sustainable steel reinforced HPFRCC structures.

1 INTRODUCTION

The design and construction of civil infrastructure that is environmentally, socially, and economically sustainable over its full life cycle, from extraction of raw construction materials to end of life management, is increasingly desirable worldwide [*e.g.* 1,2,3]. As a set of systems that support our quality of life and enable global development and progress, while consuming vast amounts of material resources and energy, it is essential that civil infrastructure is designed according to broad, long term design goals for the benefit of our planet and the current and future generations of humans, animals, and plants that will call it home.

In an effort to meet this grand sustainability challenge, numerous researchers are developing new cementitious construction materials that reduce impact on the environment. One

subset of these new materials focuses on reducing the impact of material acquisition, for instance the replacement of cement with naturally occurring or industrially produced supplementary cementitious materials [*e.g.* 4,5,6]. Another subset of these new materials focuses on reducing the material impact at the end-of-life, or reusing waste from previous construction sites through closed-loop or open-loop recycling [*e.g.* 7,8,9,10]. A third subset of new cementitious materials focuses on reducing impact and improving sustainability through improved material properties, such as durability [*e.g.* 11,12]. Extended durability of cementitious materials has proven to be particularly important for applications with long operational phases and high user impacts such as bridges and pavements [13,14,15].

Working along these lines, high-performance fiber reinforced cementitious composites (HPFRCCs), or strain hardening cementitious composites (SHCCs), have been designed to exhibit superior mechanical performance over traditional concrete materials through the formation of multiple cracks. Some research efforts have focused on the creation of HPFRCCs using industrial waste materials [16,17,18,19] to reduce material acquisition impacts. HPFRCC materials have also been designed with enhanced durability when compared to conventional concrete materials, achieved through the formation of multiple, closely spaced microcracks rather than widely spaced, localized macrocracks [20,21,22,23]. When reinforced with steel bars for structural applications, HPFRCC materials and members have exhibited improved durability in experimental tests [24,25,26].

While experimental findings that demonstrate greater durability of steel reinforced HPFRCC materials in corrosive environments are compelling, the underlying mechanism of this greater durability has only been hypothesized in the literature. Researchers have proposed that the formation of closely spaced multiple cracks, rather than widely spaced localized cracks, result in the development of more uniform corrosion, which occurs at a slower rate [25,26]. But there has yet to be an extensive effort to numerically model this hypothesis and test its validity.

Using a newly developed multi-physics transport, corrosion, and cracking model, which models these phenomena as a coupled physiochemical processes, the role of HPFRCC multiple cracking in regulating steel reinforcing bar corrosion is investigated. This model describes transport of water and chemical species, the electric potential distribution in the HPFRCC, the electrochemical propagation of steel corrosion, and the role of microcrack presence in the HPFRCC. This numerical modeling approach provides an indication of the fundamental mechanisms by which steel reinforced HPFRCC materials may be more durable than reinforced concrete and other tension-softening cementitious composites. Ultimately, the results provide greater insight into the assessment and design of more sustainable steel reinforced HPFRCC structures.

2 MULTI-PHYSICS CORROSION MODELING OF STEEL REINFORCED CEMENTITOUS MATERIALS

The framework of the integrated multi-physics modeling approach combines coupled transport of heat and matter, reinforcement corrosion, and corrosion-induced concrete damage. Initially, the transport and distribution of heat and matter is solved, along with the corrosion potential and corrosion current density. Information on the distribution of heat, matter, corrosion potential, and corrosion current density are subsequently used to simulate corrosion-induced concrete damage, *i.e.* corrosion-induced deformations and cracking. Finally, the influence of corrosion-induced deformations and cracks is taken into account in a looped simulation of heat, matter, and reinforcement corrosion.

To model initiation and propagation of reinforcement corrosion in concrete structures, a physio-chemical corrosion model is created. Two equations are used to describe the electrochemical processes and determine the corrosion current density of steel embedded in concrete. The first is Laplace's equation, describing the potential distribution in the cementitious matrix, assuming electrical charge

conservation and isotropic conductivity (Equation 1).

$$\nabla^2 \varphi = 0 \tag{1}$$

where, φ is the potential. The second is Ohm's law, which is used to determine the corrosion current density if the potential distribution and resistivity of the electrolyte are known (Equation 2) [27].

$$i_{corr} = \frac{1}{\rho_{el}} \frac{\partial \varphi}{\partial n} \tag{2}$$

where, i_{corr} is the corrosion current density, ρ_{el} is the concrete resistivity, and n is the equipotential. Kinetics of the electrochemical processes are described by anodic and cathodic polarization curves, which are comprised of both activation (Equations 3-4) and concentration polarization (Equations 5-7).

$$i_A = i_{0,A} \gamma_A \tag{3}$$

$$\gamma_A = exp\left(ln10 \frac{\varphi_A - \varphi_{0,A}}{b_A}\right) \tag{4}$$

$$i_C = i_{0,C} \frac{1 - \gamma_C}{1 + \frac{i_{o,C}}{i_{Lim} \gamma_C}} \tag{5}$$

$$\gamma_C = exp\left(-ln10 \frac{\varphi_C - \varphi_{0,C}}{b_C}\right) \tag{6}$$

$$i_{Lim} = \frac{zF D_{O_2}}{\delta} c_{O_2} \tag{7}$$

where, i_A is the anodic polarization current density, i_C is the cathodic polarization current density, $i_{0,A}$ is the anodic exchange current density, $i_{0,C}$ is the cathodic exchange current density, i_{Lim} is the limiting current density, φ_A is the anodic corrosion potential, $\varphi_{0,A}$ is the anodic equilibrium corrosion potential, φ_C is the cathodic corrosion potential, $\varphi_{0,C}$ is the cathodic equilibrium corrosion potential, b_A and b_C are the anodic and cathodic Tafel constants, respectively, z is the valence number, F is Faraday's constant, D_{O2} is the oxygen transport coefficient, δ is the thickness of the diffusion layer, and c_{O2} is the oxygen concentration. The electrochemical processes are further coupled with transport mechanisms to account for the impact of temperature (Equations 8-9), ion transport (Equation 10-11), and relative humidity and oxygen (Equation 12) on the reinforcement corrosion process.

$$pC \frac{\partial T}{\partial t} = \nabla\left(k_{T,T} \nabla T + k_{T,pC} \nabla pC\right) \tag{8}$$

$$\begin{aligned} \frac{\partial \theta_l}{\partial p_C} = C_{pC} \frac{\partial pC}{\partial t} \\ = \nabla\left(k_{pC,pC} \nabla pC + k_{pC,T} \nabla T\right) \end{aligned} \tag{9}$$

where, pC is the log of capillary pressure, T is temperature, t is time, $k_{T,T}$ is a heat transfer coefficient as a function of temperature, $k_{T,pC}$ is a heat transfer coefficient as a function of the log of capillary pressure, θ_l is the moisture content, p_C is the capillary pressure, C_{pC} is the moisture capacity, $k_{pC,pC}$ is a capillary pressure coefficient as a function of the log of capillary pressure, and $k_{pC,T}$ is a capillary pressure coefficient as a function of temperature.

$$\begin{aligned} \frac{\partial c_i}{\partial t} \\ = \nabla\left(D_i \nabla c_i + z_i u_{m,i} F c_i \nabla \varphi - c_i v\right) + R_i \end{aligned} \tag{10}$$

$$u_{m,i} = \frac{z_i F}{RT} \tag{11}$$

where, c_i is the ionic concentration of each ion considered (Cl^-, OH^-, SO_4^{2-}, Ca^{2+}, Na^+, K^+), D_i is the diffusion coefficient of each ion, z_i is the ionic valence number, $u_{m,i}$ is the ionic mobility of each ion, v is the velocity of each ion (obtained from the moisture transport model), and R is the universal gas constant.

$$D_{O_2} = 1.92 \cdot 10^{-6} \theta_{por} (1 - RH)^{2.2} \tag{12}$$

where, θ_{por} is the porosity, and RH is the relative humidity.

To link initiation and propagation of reinforcement corrosion, a conditional statement is defined along the reinforcement surface, which comprises the definition of a critical chloride threshold (Equation 13).

$$State_{reinf} = \begin{cases} i_A \; for \; c_{cl} \geq c_{crit} \\ i_C \; for \; c_{cl} < c_{crit} \end{cases} \tag{13}$$

where, $State_{reinf}$ is an anodic or cathodic state of the reinforcement, c_{cl} is the chloride con-

centration at the surface of the reinforcement, and c_{crit} is the critical chloride concentration for depassivation. When the critical chloride concentration for an element along the reinforcement surface is reached, the element becomes anodic, while the rest of the reinforcement surface stays cathodic. More detailed information on the applied modeling techniques used to describe the transport of heat and matter and reinforcement corrosion can be found in [28,29] and [30,31], respectively.

For determination of the corroded reinforcement section, Faraday´s law (Equation 14) is used to relate the thickness reduction per time unit to the corrosion current density (calculated using Equation 2).

$$X(t) = \frac{M}{zF\rho_{reinf}} \int_0^t i_{corr}(t)dt \qquad (14)$$

where $X(t)$ is the cross sectional reduction of the reinforcement as a function of time, t, M the molar mass of the reinforcement metal, z the number of electrons transferred in the half-cell reaction, F is Faraday's constant, and ρ_{reinf} the density of the reinforcement metal. Formation of soluble corrosion products, such as iron-chloride-complexes is not included in the model. Additional information on the general modeling approach for reinforcement corrosion can be found in Michel *et al.* [32], while details for non-uniform formation of corrosion products in the model are given in [33,34].

3 MULTI-PHYSICS CORROSION MODELING OF STEEL REINFORCED HPFRCC AND CONCRETE MEMBERS

3.1 Multi-physics corrosion modeling parameters

A number of common parameters are defined for the corrosion modeling performed in this study. The focus is a steel reinforced member that is 25cm in length, has a cover thickness over the reinforcing steel of 70mm, is exposed to an environment of 78% relative humidity, an atmospheric concentration of oxygen of 0.05kg/m3, a temperature of 20°C, and a surface chloride concentration of 2.0% by weight of cement over its entire lifetime. The multi-physics coupling parameters of relative humidity, oxygen diffusion, and moisture

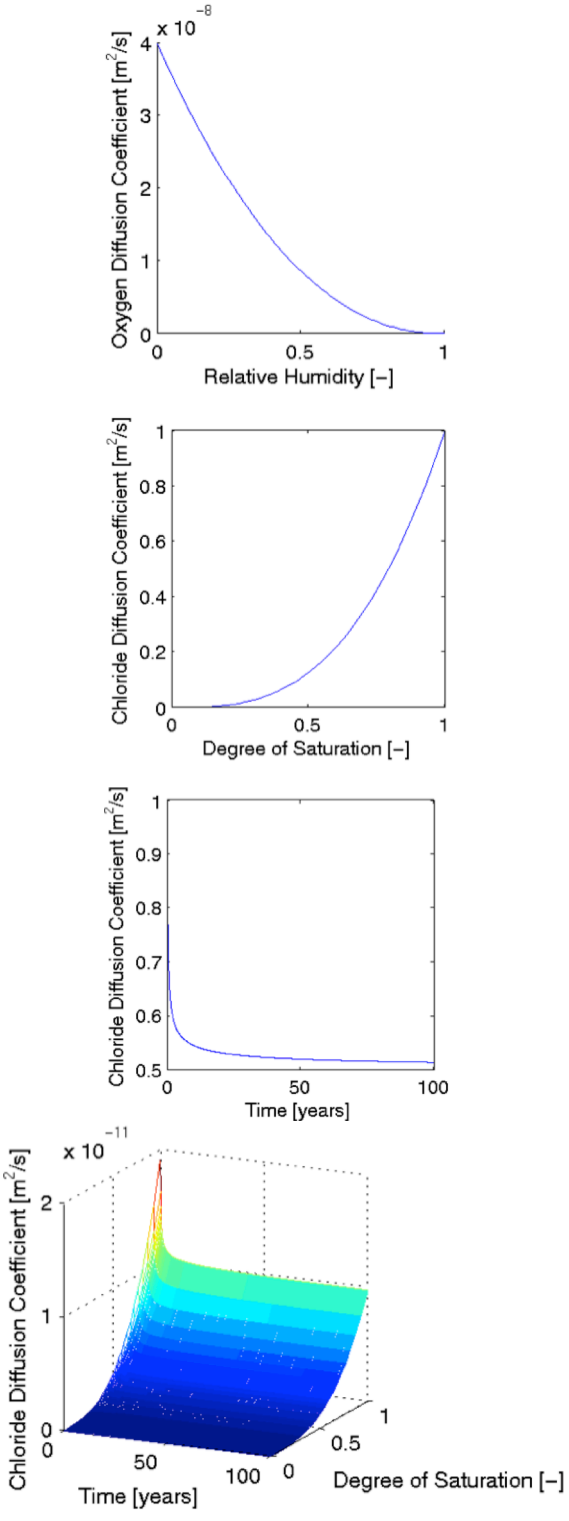

Figure 1: Multi-physics coupling of relative humidity, oxygen diffusion, and moisture in the corrosion model

are shown in Figure 1.

In addition to multi-physics coupling of

environmental parameters, a number of corrosion parameters are also coupled. This coupling includes relations among resistivity, relative humidity, current density, potential, and oxygen concentration. These relations are shown in Figure 2. For all modeling cases, member is broken up into 8 equally long annode/cathode sites, each with a randomly assigned critical chloride concentration, c_{crit}, between 0.0% and 0.4% by weight of cement. This critical concentration is used to determine the time of depassivation, and formation of an annode, using Equation 13.

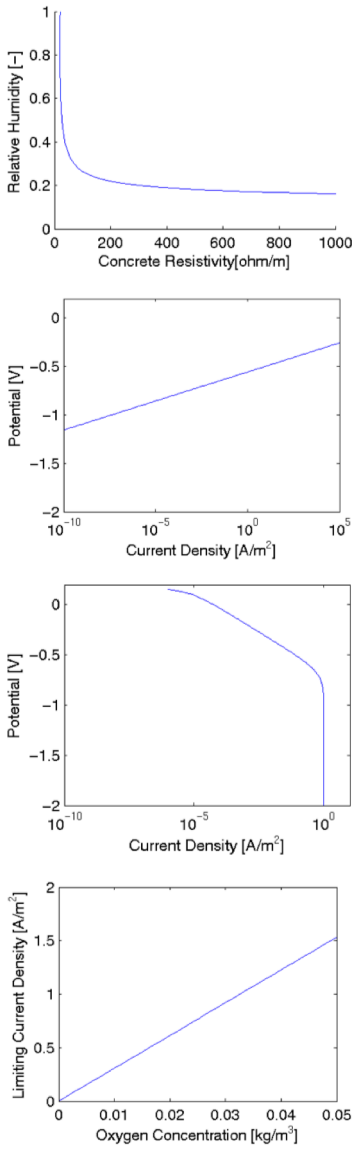

Figure 2: Multi-physics coupling of resistivity, relative humidity, current density, potential, and atmospheric oxygen concentration in the corrosion model

3.2 Modeling of an uncracked steel reinforced concrete member

As a baseline case, an uncracked, steel reinforced concrete member was modeled from initial exposure of surface chlorides, throughout the ion diffusion and transport phase, through depassivation, and into active corrosion for a time of 280 months. The distribution of chloride concentration, oxygen consumption, potential, and corrosion current are shown in Figure 3 at a time of 200 months.

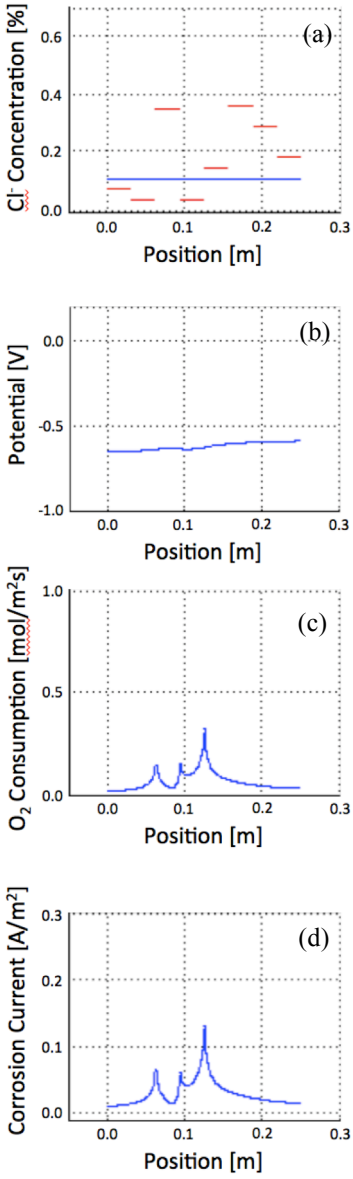

Figure 3: Distribution along the uncracked reinforced concrete member of (a) Cl^- ion concentration at the rebar surface, (b) potential, (c) O_2 consumption, and (d) corrosion current at 200 months

As expected due to the uncracked nature of the cover, the movement of chloride ions from the surface down to the level of reinforce is uniform (shown at an age of 200 months in Figure 3a). Due to the random variation of critical chloride concentrations along the length of the beam, three sites (located 0.0cm-3.125cm, 3.125cm-6.25cm, and 9.375cm-12.5cm along the beam) are depassivated and anode sites have formed. At an age of 200 months, the remainder of the reinforcement remains a cathodic reaction site. As shown in Figure 3c and 3d, the oxygen consumption and corrosion current spike at the interface between anodic and cathodic reaction sites, indicating the areas of most active corrosion along the member.

Integrating the corrosion current at each location along the beam over the 280-month modeling timeline (Equation 14), the reinforcement diameter loss at the critical section (*i.e.* section exhibiting the greatest diameter loss) and the reinforcement diameter loss along the member are plotted. These plots are shown in Figure 4.

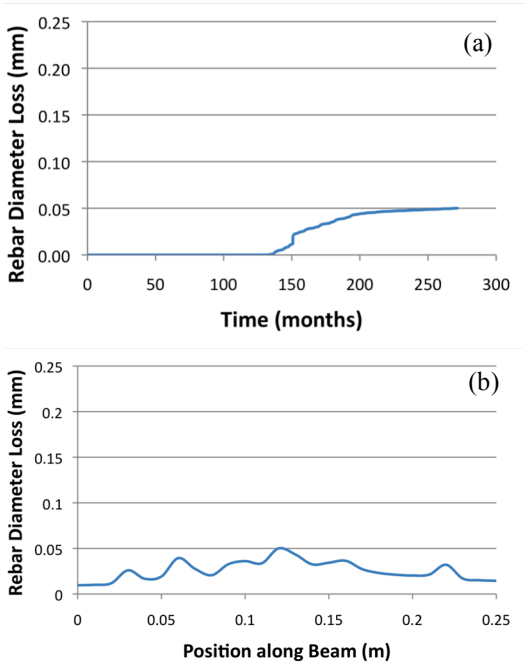

Figure 4: (a) Reinforcement diameter loss at critical section versus time and (b) reinforcement diameter loss along the uncracked reinforced concrete member at 280 months

The reduction of reinforcement diameter at the critical cross section over time, and the loss of metal along the member, follow expected trends. During transport, depassivation, and corrosion initiation, there is no loss of reinforcement diameter at the critical section (Figure 4a). Beginning at an age of approximately 140 months, active corrosion begins and progresses rapidly up until an age of approximately 200 months, at which time a significant portion of the reinforcing bar is depassivated and serves as an anodic reaction site. With fewer cathodic reaction sites to couple with an increasing number of anodic reaction sites, the corrosion rate slows. In this small-scale simulation, the corrosion reaction eventually slows to an imperceptible rate as nearly all reaction sites depassivate and flip to an anodic state.

As shown in Figure 4b, the reinforcement diameter loss along the member is reasonably uniform in nature, with the critical section (*i.e.* section of greatest diameter loss) located at mid-length. This location of the critical section is primarily due to the adjacency of the 9.375cm-12.5cm anode to a group of reaction sites that exhibit comparatively higher critical chloride concentrations (from 12.5cm-25cm along the member). These higher critical chloride concentrations preserve the cathodic nature of the 12.5cm-25cm reaction sites longer into the simulation and allowed for larger corrosion currents to occur over a longer timespan at mid-length.

3.3 Modeling of Pre-cracked Steel Reinforced Concrete

For comparison to the baseline uncracked concrete case, a pre-cracked, steel reinforced concrete member is modeled from initial exposure of surface chlorides, throughout the ion diffusion and transport phase, through depassivation, and into active corrosion for a time of 350 months. The pre-crack is placed a mid-length (*i.e.* 12.5cm from either end) with a depth of 30mm and a width of 0.1mm. The distribution of chloride concentration, oxygen consumption, potential, and corrosion current are shown in Figure 5, analogous to Figure 3,

at a time of 200 months after initial exposure of surface chlorides.

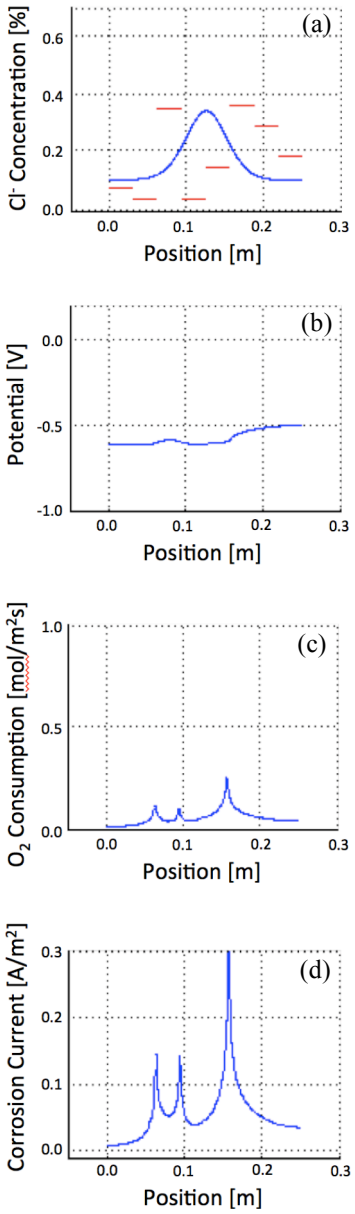

Figure 5: Distribution along the cracked reinforced concrete member of (a) Cl^- ion concentration at the rebar surface, (b) potential, (c) O_2 consumption, and (d) corrosion current at 200 months

As expected due to the cracked cover, the movement of chloride ions from the surface down to the level of reinforcement is non-uniform, with faster transport occurring through and around the crack at mid-length (shown at an age of 200 months in Figure 5a). Regardless of the random nature of critical chloride concentrations along the length of the member, the uneven diffusion front the center of the member causes depassivation long before either end of the member, thus creating a strong couple of anodic reaction sites at mid-length and cathodic reaction sites at the member ends. This couple remains present throughout most of the simulation timespan.

Summing the corrosion current at each location along the beam over the 350 month modeling timeline (Equation 14), the reinforcement diameter loss at the critical section (*i.e.* the section exhibiting the most diameter loss along the member length) and the reinforcement diameter loss along the member are plotted. These two plots are shown in Figure 6.

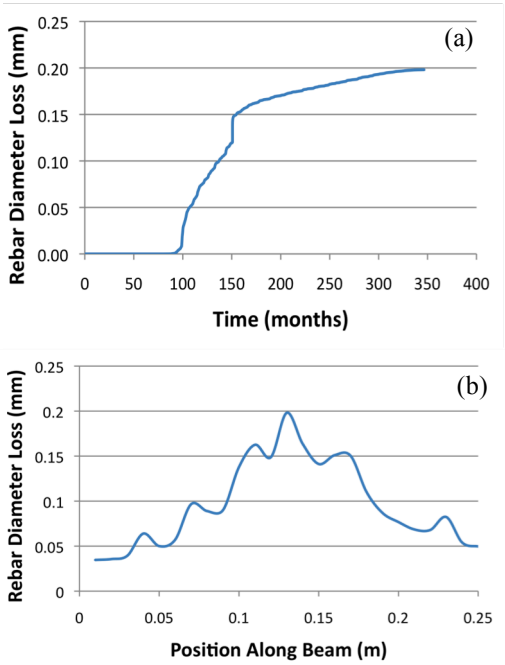

Figure 6: (a) Reinforcement diameter loss at critical section over time and (b) reinforcement diameter loss along the cracked reinforced concrete member at 350 months

Once again, the reduction of diameter at the critical cross section over time, and the loss of metal along the member, follow an expected trend. During transport, depassivation, and corrosion initiation, there is no loss of reinforcement diameter at the critical section (Figure 6a). Beginning at an age of approximately 90 months, active corrosion begins and progresses (rapidly at times) up until the end of the simulation. As compared to the uncracked concrete, there is a shorter depassivation and initiation time due to pres-

ence of 30mm deep cracks. Thus, there is significantly greater rebar diameter lost at 200 months (0.05mm in uncracked concrete versus 0.17mm in cracked concrete). Additionally the corrosion continues for a longer duration, only beginning to plateau after 350 months of simulation.

As shown in Figure 6b, the reinforcement diameter loss along the member is more concentrated at the critical section (*i.e.* section of greatest diameter loss) located at mid-length. This location of the critical section is primarily due to the earlier depassivation at mid-length due to the crack presence, and a longer duration of the anode/cathode couple. Moreover, the comparison of Figure 4b and Figure 6b confirm the numerical ability of the corrosion model to capture the localized effects of cracking on corrosion initiation and propagation phenomena over time.

3.4 Modeling of Pre-cracked Steel Reinforced HPFRCC

For comparison to the baseline uncracked concrete case and the cracked concrete case, a pre-cracked, steel reinforced HPFRCC member is modeled from initial exposure of surface chlorides, throughout the ion diffusion and transport phase, through depassivation, and into active corrosion for a time of 360 months. A series of 5 microcracks are placed at 5cm intervals along the member, with a depth of 30mm and a width of 0.1mm. The distribution of chloride concentration, oxygen consumption, potential, and corrosion current are shown in Figure 7, analogous to Figure 3 and Figure 5, at a time of 200 months after initial exposure of surface chlorides.

Unlike the cracked concrete case, the movement of chloride ions from the surface down to the level of reinforcement is nearly uniform, and more similar to the uncracked concrete, due to the presence of multiple cracks enabling uniformly faster transport along the entire member length (shown at an age of 200 months in Figure 7a). Similar to the uncracked concrete case, the random nature of the critical chloride concentration along the member length results in neighboring anode and cathode reaction sites, resulting in more uniform corrosion propagation. At an age of 200 simulation months, most of the member has depassivated and few anode/cathode couples remain to promulgate ongoing corrsion (as seen in Figure 7d).

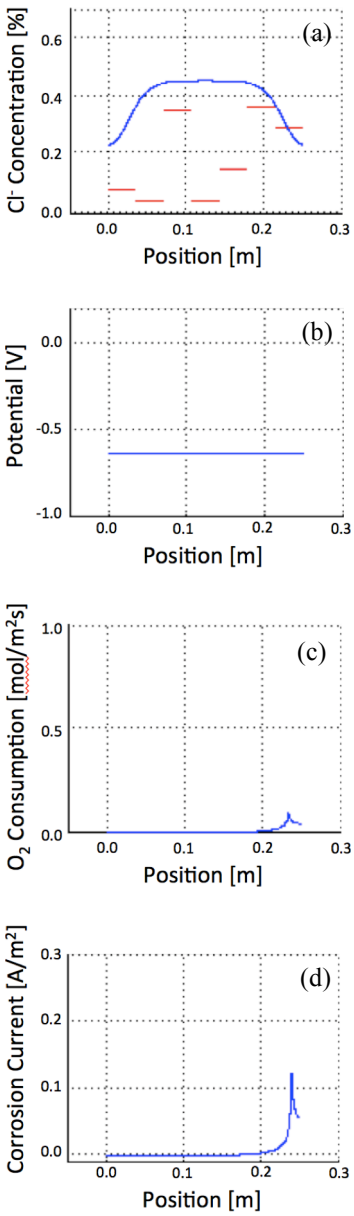

Figure 7: Distribution along the cracked reinforced HPFRCC member of (a) Cl^- ion concentration at the rebar surface, (b) potential, (c) O_2 consumption, and (d) corrosion current at 200 months

Once again, summing the corrosion current at each location along the beam over the 360 month modeling timeline (Equation 14), the reinforcement diameter loss at the critical section (*i.e.* section exhibiting the greatest diame-

ter loss) and the reinforcement diameter loss along the member are plotted (Figure 8).

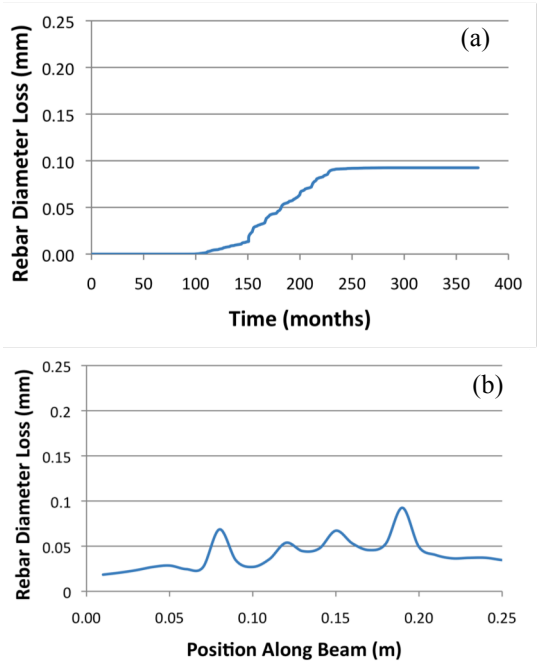

Figure 8: (a) Reinforcement diameter loss at critical section over time and (b) reinforcement diameter loss along the cracked reinforced HPFRCC member at 360 months

Unlike the uncracked and cracked concrete, the reduction of diameter at the critical cross section over time and the loss of metal along the member follow an unexpected trend. As before, during transport, depassivation, and corrosion initiation, there is no loss of reinforcement diameter at the critical section (Figure 8a). The depassivation and initiation time is similar to that for cracked concrete. Beginning at an age of 100 months, active corrosion begins and progresses (in a more controlled manner than for cracked concrete) only for the next 120 months. There is only moderate diameter loss at 200 months (0.07mm in cracked HPFRCC versus 0.17mm in cracked concrete), which is much closer to the uncracked concrete case (0.05mm in uncracked concrete).

As shown in Figure 8b, the reinforcement diameter loss along the member is less concentrated at the critical section (*i.e.* section of greatest diameter loss) than for the cracked concrete. Overall the modeling response is more similar to the uncracked concrete member than the cracked concrete member.

4 DISCUSSION

The numerical modeling results of this study fit well with previous experimental conclusions drawn by other researchers. For instance, Miyazato and Hiraishi investigated the initiation and propagation of corrosion in pre-cracked reinforced concrete and pre-cracked steel reinforced ECC beams [24]. In their experiments, Miyazato and Hiraishi found localized corrosion in pre-cracked reinforced concrete members to be centered around the location of the pre-crack, with relatively little reinforcement section loss away from the pre-crack (Figure 9). This localization phenomenon is observed numerically in Figure 6b. As seen in Figure 5, the underlying mechanism is localized depassivation and a strong anode/cathode couple forming between the cracked and uncracked portions of the reinforced concrete member.

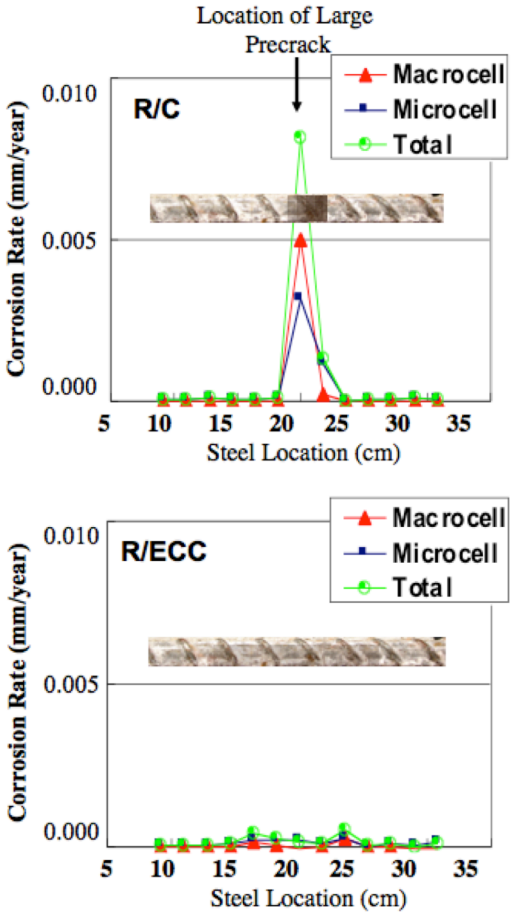

Figure 9: Corrosion rate along (top) a pre-cracked reinforced concrete beam (*i.e.* single crack) and (bottom) a pre-cracked reinforced HPFRCC beam (*i.e.* multiple cracks), adapted from [24]

Miyazato and Hiraishi found that uniform corrosion formed in reinforced HPFRCC beams with multiple cracking. Additionally the maximum corrosion rate (mm/diameter loss) in cracked reinforced HPFRCC beams was much lower. Their proposed hypothesis for this slow, uniform corrosion was the formation of many small anode/cathode couples around each crack, rather than one concentrated anode/cathode couple as in the cracked reinforced concrete. Together, Figure 7 and Figure 8 can be interpreted as the first numerical observation of the Miyazato and Hiraishi hypothesis.

Connecting the results of this paper to sustainability of built environment, the extension of service life through the use of highly durable infrastructure materials, such as HPFRCCs, can lead to significant sustainability improvements of civil infrastructure [35]. Lepech *et al.* showed that in repair applications, by accounting for the greater durability of HPFRCC materials the cumulative environmental impacts of HPFRCC repairs over a bridge infrastructure's 100-year life cycle can be more than 30% lower when compared to traditional concrete repairs technologies.

5 CONCLUSION

While opportunities for HPFRCC materials to reduce sustainability impacts of the built environment are promising, the fundamental mechanisms that extend the service life of steel reinforced HPFRCC materials must be well understood. This study represents the first multi-physics modeling effort to explain the fundamental mechanisms that lead to more uniform, slower corrosion rates in steel reinforced HPFRCC members as compared to reinforced concrete members. The mechanisms identified in this numerical study include (i) the formation of a more uniform chloride diffusion front in multiple-cracked steel reinforced HPFRCC materials, and (ii) a more uniform formation of smaller anode/cathode reaction couples along the length of the steel reinforced HPFRCC member as compared to a reinforced concrete member. These two mechanisms work together to result in slower, more uniform corrosion in cracked steel reinforced HPFRCC members when compared to cracked reinforced concrete members, as observed experimentally by Miyazato and Hiraishi.

There are a number of important limitations associated with this modeling study, and therefore a number of lines of future work remain. A significant limitation of the current modeling approach is that it examines a finite beam rather than a complete structure. This is significant since once the critical chloride concentration is surpassed at the surface of the reinforcement, the cathodic site automatically becomes an anodic site (Equation 13). Ultimately, this results in an entirely anodic member of finite length, which artificially limits ongoing corrosion that would normally be experienced by a full-scale structure. Additionally, only 8 anode or cathode sites are assumed along the member in this study. Currently, there is no published literature that discusses the observed length of anodic or cathodic sites on corroding steel reinforcement. Finally, this numerical study has yet to be validated using the exact experimental conditions of tests run by Miyazato and Hiraishi [24], Kobayashi and Rokugo [25], or Sahmaran *et al.* [26]. Such validation is the next step in model development and refinement and comprises ongoing work by the researchers.

6 ACKNOWLEDGMENTS

The authors gratefully acknowledge the financial support of the Stanford Blume Fellowship, the Stanford Shah Family Fellowship, the Stanford-Terman Faculty Fellowship, the Danish Expert Centre for Infrastructure Constructions, and COWIfonden. The authors also thank the support of project 'Sustainable Rehabilitation of Civil and Building Structures' funded by the Nordic Innovation Centre, Project No. 08190 SR. Finally, this material is partially based upon work supported by the US National Science Foundation under "CAREER: Multi-physics Modeling for Probabilistic Design and Engineering of Sustainable Infrastructure", Grant No. 1453881. Any opinions, findings, and conclusions or recommen-

dations expressed in this material are those of the authors and do not necessarily reflect the views of the US National Science Foundation.

REFERENCES

[1] Minsker, B., Baldwin, L., Crittenden, J., Kabbes, K., Karamouz, M., Lansey, K., Malinowski, P., et al. "Progress and recommendations for advancing performance-based sustainable and resilient infrastructure design." *Journal of Water Resources Planning and Management* 141, no. 12 (2015): A4015006.

[2] Li, R., Du, H. "Sustainable Construction Waste Management in Australia: A Motivation Perspective." In *Construction Safety and Waste Management*, pp. 1-30. Springer International Publishing, 2015.

[3] Bhattacharya, A., Oppenheim, J., Stern, N. (2015) "Driving sustainable development through better infrastructure: Key elements of a transformation program." Global Economy & Development Working Paper 91.

[4] Davidovits, J. (2013). Geopolymer cement. A review. *Geopolymer Institute, Technical papers*, 21, 1-11.

[5] Jamieson, E., McLellan, B., van Riessen, A., Nikraz, H. (2015). Comparison of embodied energies of Ordinary Portland Cement with Bayer-derived geopolymer products. *Journal of Cleaner Production*, 99, 112-118.

[6] Wilkinson, A., Woodward, D., Magee, B., Tretsiakova-McNally, S. (2015). A state of the art review into the use of geopolymer cement for road applications. *Bituminous Mixtures and Pavements VI*, 147.

[7] Thomas, C., Setién, J., Polanco, J. A., Alaejos, P., De Juan, M. S. (2013). Durability of recycled aggregate concrete. *Construction and Building Materials*, 40, 1054-1065.

[8] Radonjanin, V., Malešev, M., Marinković, S., Al Malty, A. E. S. (2013). Green recycled aggregate concrete. *Construction and Building materials*, 47, 1503-1511.

[9] Xiao, J., Li, W., Fan, Y., Huang, X. (2012). An overview of study on recycled aggregate concrete in China (1996–2011). *Construction and Building Materials*, 31, 364-383.

[10] Behera, M., Bhattacharyya, S. K., Minocha, A. K., Deoliya, R., Maiti, S. (2014). Recycled aggregate from C&D waste & its use in concrete–A breakthrough towards sustainability in construction sector: A review. *Construction and building materials*, 68, 501-516.

[11] Naik, T. R., Canpolat, F., & Moriconi, G. (2015). Sustainability And High-Performance Of Concrete–A Review. ACI Special Publication, Volume 305, pp. 43.1-43.10.

[12] Hooton, R. D., Bickley, J. A. (2014). Design for durability: the key to improving concrete sustainability. *Construction and Building Materials*, 67, 422-430.

[13] Keoleian, G. A., Kendall, A., Dettling, J. E., Smith, V. M., Chandler, R. F., Lepech, M. D., Li, V. C. (2005). Life cycle modeling of concrete bridge design: Comparison of engineered cementitious composite link slabs and conventional steel expansion joints. *Journal of infrastructure systems*, 11(1), 51-60.

[14] Zhang, H., Lepech, M. D., Keoleian, G. A., Qian, S., & Li, V. C. (2009). Dynamic life-cycle modeling of pavement overlay systems: Capturing the impacts of users, construction, and roadway deterioration. *Journal of Infrastructure Systems*, 16(4), 299-309.

[15] Zhang, H., Keoleian, G. A., Lepech, M., & Kendall, A. (2010). Life-cycle optimization of pavement overlay systems. *Journal of infrastructure systems*, 16(4), 310-322.

[16] Lepech, M., Li, V. C., Robertson, R. E., & Keoleian, G. A. (2008). Design of green engineered cementitious composites for improved sustainability. *ACI Materials Journal*, 105(6), 567-575.

[17] Yang, E. H., Yang, Y., & Li, V. C. (2007). Use of high volumes of fly ash to improve ECC mechanical properties and material greenness. *ACI Materials Journal*, 104(6), 620-628.
[18] Kendall, A., Keoleian, G. A., Lepech, M. (2008). Materials design for sustainability through life cycle modeling of engineered cementitious composites. *Materials and Structures*, 41(6), 1117-1131.
[19] Huang, X., Ranade, R., Ni, W., & Li, V. C. (2013). Development of green engineered cementitious composites using iron ore tailings as aggregates. *Construction and Building Materials*, 44, 757-764.
[20] Şahmaran, M., Li, V. C. (2009). Durability properties of micro-cracked ECC containing high volumes fly ash. *Cement and Concrete Research*, 39(11), 1033-1043.
[21] Lepech, M., Li, V. C. (2006). Long term durability performance of engineered cementitious composites. *Restoration of Buildings and Mon.*, 12(2), 119-132.
[22] Li, V. C., Horikoshi, T., Ogawa, A., Torigoe, S., Saito, T. (2004). Micromechanics-based durability study of polyvinyl alcohol-engineered cementitious composite. *ACI Materials Journal*, 101(3), 242-248.
[23] Li, V. C. (2004). High performance fiber reinforced cementitious composites as durable material for concrete structure repair. *International Journal for Restoration*, 10(2), 163-180.
[24] Miyazato, S., Hiraishi, Y. (2013). Durability against Steel Corrosion of HPFRCC with Bending Cracks. *J of Advanced Concrete Technology*, 11(4), 135-143.
[25] Kobayashi, K., Rokugo, K. (2013). Mechanical performance of corroded RC member repaired by HPFRCC patching. *Const. and Building Mat.*, 39, 139-147.
[26] Sahmaran, M., Li, V. C., Andrade, C. (2008). Corrosion resistance performance of steel-reinforced engineered cementitious composite beams. *ACI Materials Journal*, 105(3), 243-250.
[27] J. Warkus, et al. (2006) Numerical modeling of corrosion - Theoretical backgrounds, *Material Corrosion*, 57:614-617.
[28] Flint, M., Michel, A., Billington, S., Geiker, M. (2014) "Influence of temporal resolution and processing of exposure data on modeling of chloride ingress and reinforcement corrosion in concrete" *Materials and Structures*, 47, 4:729-748.
[29] Pease, B. J., Michel, A., Geiker, M. R., Stang, H. (2012) "Modelling Moisture Ingress through Simplified Concrete Geometries", In: Proceedings of ICDC, June 17-21, 2012, Trondheim, Norway.
[30] Michel, A., Geiker, M. R., Stang, H., Olesen, J. F. (2010) "Numerical modelling of reinforcement corrosion in concrete structures", In: Proceedings of 8th fib PhD Symposium, June 20-23, 2010, Copenhagen, Denmark.
[31] Michel, A., Geiker, M. R., Stang, H., Olesen, J. F. (2012). "Modelling reinforcement corrosion in concrete." In Proceedings of 2nd International Conference on Microstructure Related Durability of Cementitious Composites. April 11-13, Delft, Netherlands.
[32] Michel, A., M.R. Geiker, H. Stang, M. Lepech (2013) "Integrated modeling of corrosion-induced deterioration in reinforced concrete structures" 2013 European Corrosion Congress. Estoril, Portugal. September 1-5, 2013.
[33] Thybo, A. E. A., Michel, A., Stang, H. (2013) "Modeling of Corrosion-induced Concrete Damage" In: Proceedings of FraMCos 8, March 10-14, 2013, Toledo, Spain.
[34] Thybo, A. E. A., Michel, A., Stang, H. (2013) "Sustainability assessment of concrete structure durability under reinforcement corrosion" In: Proceedings of ICCS13, May 27-29, 2013, Tokyo, Japan.
[35] Lepech, M., Stang, H., Geiker, M. (2011) "Integrated Probabilistic Life Cycle Assessment and Durability Design for Sustainable SHCC Infrastructure" In Proceedings of 2nd RILEM International Workshop on Strain Hardening Cementitious Composites (SHCC2). December 14-12, 2011. Rio de Janeiro, Brazil.